Applied Catalysis B: Environmental 183 (2016) 269–281

Contents lists available at ScienceDirect

Applied Catalysis B: Environmental

journal homepage: www.elsevier.com/locate/apcatb

Promotional effects of zirconium doped $CeVO_4$ for the low-temperature selective catalytic reduction of NO_x with NH_3

Xin Zhao [a], Lei Huang [a,*], Hongrui Li [a], Hang Hu [a], Xiaonan Hu [a], Liyi Shi [a,b], Dengsong Zhang [a,*]

[a] Research Center of Nano Science and Technology, Shanghai University, Shanghai 200444, PR China
[b] Department of Chemistry, Shanghai University, Shanghai 200444, PR China

ARTICLE INFO

Article history:
Received 12 August 2015
Received in revised form 13 October 2015
Accepted 28 October 2015
Available online 31 October 2015

Keywords:
Selective catalytic reduction
Zr doped
$CeVO_4$
Vanadates
$deNO_x$

ABSTRACT

In this work, we developed a novel zirconium doped $CeVO_4$ to form $Ce_{1-x}Zr_xVO_4$ (x = 0.05, 0.10, 0.15, 0.20, 0.30, 0.50, 0.70, 0.80) solid solution as a low-temperature catalyst for the selective catalytic reduction (SCR) of NO_x with NH_3. The optimized catalysts showed excellent performance at low temperature. The light-off temperature (the temperature at which the conversion of NO reaches 50%) was down to about 125 °C, while the temperature window (the NO conversion is above 80%) ranged from 150 to 375 °C. The selectivity was kept close to 100% during the whole temperature range. Furthermore, the catalysts also exhibited good H_2O/SO_2 durability and fascinating performance at high gas hourly space velocity of 400,000 h^{-1}. Hydrogen temperature-programmed reduction, X-ray photoelectron spectroscopy, ammonia and nitrogen oxides temperature-programmed desorption and *in-situ* diffuse reflectance infrared Fourier transform experiments were performed to study the influence of Zr doping on the SCR performance. It was found that the introduction of Zr in $CeVO_4$ with a proper amount could significantly increase the surface area, oxidative ability, active oxygen species and especially surface acid sites of the catalysts, which were beneficial to the promotion of SCR performance.

1. Introduction

Selective catalytic reduction (SCR) has been proved to be one of the most effective technologies to control the emission of nitrogen oxides (NO_x) which has caused the environmental issues including acid rain, global warming, ozone depletion and etc [1–8]. As one of the most effective SCR catalysts, vanadium-based catalysts display adequate activity typically at 300–400 °C and are widely used in stationary sources [9–13]. However, this catalyst still suffers from the volatility and toxicity of VO_x and the easy deactivation. For example, the high concentration of ash and SO_2 in the flue gas reduces their performance and longevity. An attractive option to solve this problem is to place the SCR unit downstream of the electrostatic precipitators and desulfurizer where the temperature decreased to below 200 °C or even lower [14–17]. Here, low-temperature SCR catalysts are required to avoid reheating of the flue gas, thus decreasing the cost. Therefore, the development of low-temperature SCR catalysts with high NO_x conversion, good N_2 selectivity, low cost and strong stability is of great interest for industrial application.

Recently, low-cost vanadates which are free of tungsten and molybdenum species attracted intensive attention due to its great performance in the SCR of NO_x [18–23]. Especially, the melting point of vanadates (780 °C for copper vanadate, 850 °C for iron vanadate, 1030 °C for manganese vanadate, etc.) are normally higher than that of V_2O_5 (only 690 °C), implying that the thermal stability of vanadium species as vanadates might be better than as V_2O_5. For example, Casanova and co-workers reported a series of rare earth vanadates supported over TiO_2–WO_3–SiO_2, which exhibited an excellent $deNO_x$ activity and a prominent thermal stability [24]. Liu et al., reported iron vanadate on TiO_2 which showed good activity, N_2 selectivity, high thermal stability and H_2O/SO_2 durability in NH_3-SCR reactions. The electronic inductive effect between Fe^{3+} and V^{5+} species was proved to be effective for decreasing the unwanted unselective oxidation of NH_3, thus promoting the high N_2 selectivity at high temperatures [18]. In our previous work, we also found that the vanadates with different morphologies, such as nanosheets and one-dimensional (1-D) nanostructures were effective and stable for De-NO_x application [19,20]. Therefore, the vanadates might be a candidate of SCR cata-

* Corresponding authors. Fax: +86 21 66136079.
E-mail addresses: leihuang@shu.edu.cn (L. Huang), dszhang@shu.edu.cn (D. Zhang).

http://dx.doi.org/10.1016/j.apcatb.2015.10.052
0926-3373/

lysts for industrial application and are worth being studied deeply. In fact, for all those reported vanadates based catalysts, the light-off temperatures (the temperature at which the conversion of NO reaches 50%) were higher than 180 °C, while the temperature window for 80% NO conversion normally ranged from 225 to 400 °C [18–20,24,25]. Obviously, this temperature range can't meet the requirements of low-temperature SCR catalysts.

In this work, we developed a novel zirconium doped $CeVO_4$ ($Ce_{1-x}Zr_xVO_4$) for the low-temperature SCR of NO_x with NH_3. The light-off temperature was down to about 125 °C, while the temperature window ranged from 150 to 375 °C with the N_2 selectivity almost close to 100%. Besides, this catalyst also exhibited an excellent stability and a superior performance under a high GHSV of 400,000 h^{-1}. The influence of the doped zirconium on the nature of the catalyst during the SCR reactions was studied. The crystal structures and morphologies were characterized by X-ray diffraction (XRD), N_2 sorption, Transmission electron microscopy (TEM), high-resolution TEM (HRTEM) and selected area electron diffraction (SAED). Besides, the redox property, surface active oxygen species and acid sites were characterized by hydrogen temperature-programmed reduction (H_2-TPR), X-ray photoelectron spectroscopy (XPS), ammonia and nitrogen oxides temperature-programmed desorption (NH_3-TPD and NO_x-TPD), and *in-situ* diffuse reflectance infrared Fourier transform (*in-situ* DRIFTS) experiments.

2. Experimental

2.1. Catalyst preparation

All the chemicals were purchased from Sinopharm Chemical Regent Company and used without further purification.

$CeVO_4$ nanorods were prepared by a simple hydrothermal synthesis method [26]. In a typical process, 3.47 g $Ce(NO_3)_3{\cdot}6H_2O$ and 2.92 g EDTA were dissolved in 25 ml deionized water. After vigorous stirring of the solution for 30 min, 25 ml aqueous solution containing 0.936 g NH_4VO_3 was added. Then the pH value of the solution was adjusted to 10.0 with a proper amount of NaOH. The mixture was transferred into a 100 ml Teflon-lined stainless steel autoclave at 180 °C for 6 h. When the autoclave was naturally cooled to room temperature, the precipitates were collected and washed several times with deionized water and anhydrous ethanol, and dried at 80 °C for 12 h.

Similar hydrothermal process was applied to prepare the Zr doped $CeVO_4$ ($Ce_{1-x}Zr_xVO_4$, x = 0.05, 0.10, 0.15, 0.20, 0.30, 0.50, 0.70, 0.80). The amounts of $Ce(NO_3)_3{\cdot}6H_2O$ used here were 3.30 g, 3.13 g, 2.96 g, 2.78 g, 2.44 g, 1.74 g, 1.04 g and 0.70 g. The corresponding amounts of $Zr(NO_3)_4{\cdot}5H_2O$ were 0.17 g, 0.34 g, 0.52 g, 0.69 g, 1.03 g, 1.72 g, 2.41 g and 2.75 g, respectively. In a typical process, $Ce(NO_3)_3{\cdot}6H_2O$ and $Zr(NO_3)_4{\cdot}5H_2O$ were firstly dissolved in 50 ml H_2O solution and vigorously stirred for a few minutes. 0.936 g NH_4VO_3 dissolved in 25 ml H_2O then was added into the stirring solution. The pH value of the solution was adjusted to 8.0 by NaOH. After that, the mixture was transferred into a 100 ml Teflon-lined stainless steel autoclave and maintained at 180 °C for 12 h. When the autoclave was naturally cooled to room temperature, the precipitates were collected and washed several times with deionized water and anhydrous ethanol, and dried at 80 °C for 12 h.

All the as-synthesized catalysts were calcined at 450 °C for 4 h in air.

2.2. Characterization

The XRD was performed on a Rigaku D/MAX-RB X-ray diffractometer by using Cu Kα (40 kv, 40 mA) radiation and a secondary beam graphite monochromator. Nitrogen adsorption–desorption isotherms of the samples were measured at −196 °C using an automated surface and pore size analyser (Autosorb-IQ2, Quantachrome Corporation), and the corresponding pore size distribution curves were calculated from desorption branches by the BJH method. The specific surface area of the samples was calculated by the Brunauer–Emmett–Teller (BET) method. TEM and HRTEM were tested on JEM-200CX and JEM-2100F, respectively. The XPS of all the elements was recorded on a PerkinElmer PHI 5000C ESCA system equipped with a dual X-ray source, using a Mg-Kα (1253.6 eV) anode and a hemispherical energy analyzer. The background pressure during data acquisition was kept below 10^{-6} Pa. All the binding energies were calibrated using contaminant carbon (C 1s = 284.6 eV) as a reference. The visible Raman spectra were recorded on an inVia-reflex Renishaw spectrometer equipped with a holographic notch filter, a CCD detector, and a laser radiating at 532 nm.

The H_2-TPR, NH_3-TPD and NO_x-TPD were conducted on TianjinXQ TP-5080 auto-adsorption apparatus, and the H_2, NH_3 and NO_x were monitored by a TCD. 80 mg of each sample was pre-treated with high-purity (99.999%) N_2 (30 ml min^{-1}) at 300 °C for 30 min before TPR or TPD tests. For H_2-TPR, after cooling to room temperature, the flowing gas was switched to 10% H_2/N_2 and the reactor temperature was raised to 850 °C at a rate of 10 °C min^{-1}. For NH_3-TPD and NO_x-TPD, after cooling down to 100 °C, the samples were exposed to a flow of NH_3 or NO_x at the same temperature for 1 h. Finally, the temperature was raised to 450 or 500 °C at a heating rate of 10 °C min^{-1}.

In-situ DRIFTS experiments were conducted from 1100 to 1900 cm^{-1} at a spectral resolution of 4 cm^{-1} (number of scans, 64) on an FTIR spectrometer (Nicolet 6700) equipped with a Harrick DRIFTS cell and a MCT/A detector. The catalysts were pre-treated at 400 °C in a flow of N_2 (50 ml min^{-1}) for 0.5 h to remove the physisorbed water and other impurities, then cooled to target temperature under N_2 flow before each experiment. Background spectra were recorded in the N_2 flow and automatically subtracted from the corresponding spectra. The reaction conditions were as follows: 500 ppm NH_3, 500 ppm NO, 5% O_2 and N_2 balance. The NH_3 pre-adsorption time was controlled as 1 h. Then, the samples were purged by N_2 for 30 min until the infrared signals were stabilized.

2.3. Activity measurements

The SCR activities were carried out in a fixed-bed quartz microreactor (i.d. 8 mm) operating in a steady state flow mode. The gas composition was as follows: 0.4 g catalysts, 500 ppm NO, 500 ppm NH_3, 5 vol% O_2, 8 vol% H_2O (when used), 200 ppm SO_2 (when used) and balance N_2. The total flow rate was 250 ml min^{-1}. Thus, the corresponding gas hourly space velocity (GHSV) was 26,000 h^{-1}. During the GHSVs test, the gas composition was as follows: 500 ppm NO, 500 ppm NH_3, 5 vol% O_2, and balance N_2. The total flow rate was 1000 ml min^{-1}. The amount of the catalyst was 0.4 g, 0.2 g and 0.1 g, respectively. Before each activity test, catalysts should be pressed, crushed and sieved to 40–60 mesh. The temperature was increased from 100 °C to 400 °C. At each temperature step the concentrations of NO, NH_3 and N_2O were obtained. The concentrations of NO in the inlet and outlet gases were measured by a 4000VM NO_x Analyzer. The concentrations of N_2O and NH_3 were measured by a G200 analyzer and IQ 350 ammonia analyzer. NO conversion and N_2 selectivity were calculated according to the following expression:

$$\text{NOconversion}\,(\%) = \frac{[\text{NO}]_{\text{in}} - [\text{NO}]_{\text{out}}}{[\text{NO}]_{\text{in}}} \times 100\%$$

$$\text{N}_2\text{selectivity} = \left(1 - \frac{2[\text{N}_2\text{O}]_{\text{out}}}{[\text{NO}_x]_{\text{in}} + [\text{NH}_3]_{\text{in}} - [\text{NO}_x]_{\text{out}} - [\text{NH}_3]_{\text{out}}}\right) \times 100\%$$

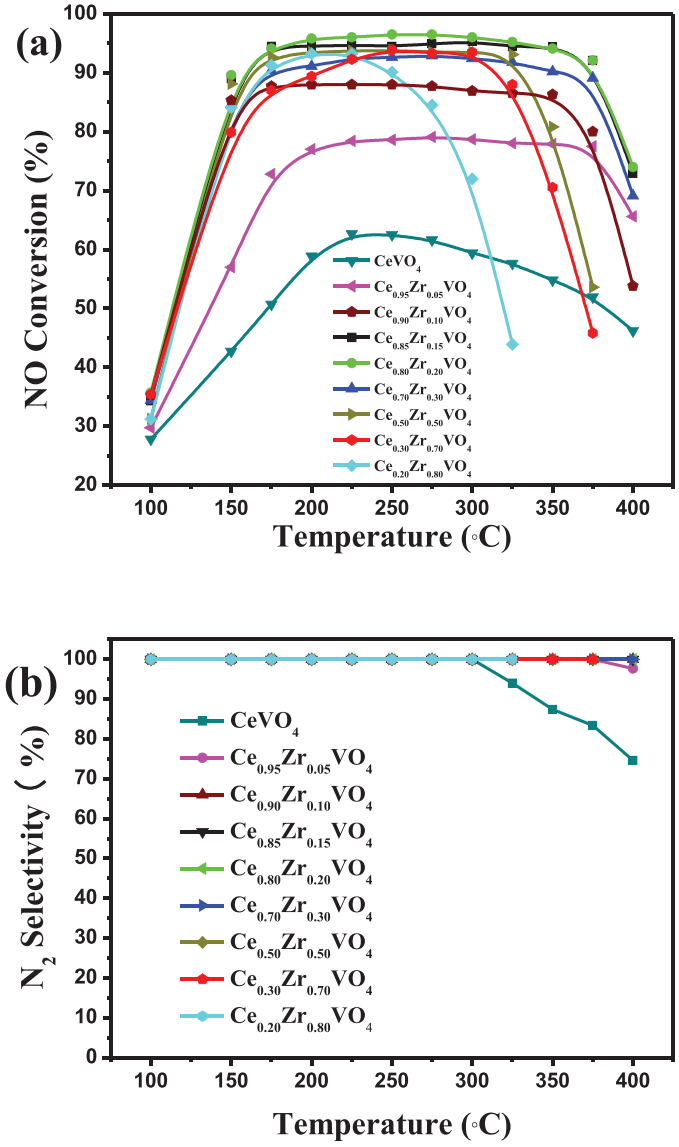

Fig. 1. (a) NO conversion and (b) N_2 selectivity in NH_3-SCR reaction as a function of temperature in the feed gas of 250 ml min^{-1} total rate over the $CeVO_4$ and $Ce_{1-x}Zr_xVO_4$ catalysts. Reaction conditions: [NO] = [NH_3] = 500 ppm, [O_2] = 5%, GHSV = 26,000 h^{-1}.

where the $[NO]_{in}$, $[NO]_{out}$, $[NO_x]_{in}$, $[NO_x]_{out}$, $[NH_3]_{in}$, $[NH_3]_{out}$ and $[N_2O]_{out}$ correspond to the inlet and outlet concentration of a steady-state, respectively. NO_x means the total concentration of NO and NO_2.

The values of the GHSV were obtained according to the following expression:

$$GHSV = \frac{q_v}{\pi h r^2}$$

where the q_v corresponds to the total flow rate, h corresponds to the height of the catalyst in the reactor and r means the radius of the reactor.

3. Results and discussion

3.1. NH_3-SCR performance under different reaction conditions

Fig. 1a shows the NO conversion over $CeVO_4$ and $Ce_{1-x}Zr_xVO_4$ catalysts with the temperature increasing from 100 °C to 400 °C. The highest NO conversion of $CeVO_4$ catalyst was only 62.5% at around 225 °C. No obvious temperature window was observed. Interestingly, the doping of Zr could significantly promote the performance of $CeVO_4$. The highest NO conversion of $Ce_{0.95}Zr_{0.05}VO_4$ catalyst increased to 79.1%, and the NO conversion above 70% was in the range of 175–375 °C. With the doping amount of Zr increasing from $Ce_{0.90}Zr_{0.10}VO_4$ to $Ce_{0.70}Zr_{0.30}VO_4$, the NO conversions of the catalysts further increased to above 95% and the temperature window above 80% was broadened to 150–375 °C. However, further increasing the Zr amount led to the decrease of SCR activity at high temperatures. The highest temperatures of the temperature window above 80% gradually decreased to 340 °C, 325 °C and 280 °C for the $Ce_{0.50}Zr_{0.50}VO_4$, $Ce_{0.30}Zr_{0.70}VO_4$ and $Ce_{0.20}Zr_{0.80}VO_4$, respectively, keeping the starting temperatures at around 150 °C.

It is well known that the conversion efficiency between 125 and 200 °C is an important factor for judging a low-temperature SCR catalyst. Obviously, with the introduction of Zr, the light-off temperature was down to about 125 °C, while the temperature window ranged from 150 to 375 °C, indicating that the $Ce_{1-x}Zr_xVO_4$ with proper amount of Zr can work as a low-temperature catalyst. Very importantly, the above performance was achieved at a wide range of Zr doping amount, implying that the $Ce_{1-x}Zr_xVO_4$ catalyst with good performance could be easily obtained during the preparation process.

The N_2 selectivity was also found promoted with the introduction of Zr, as shown in Fig. 1b. The selectivity was very high for all the $CeVO_4$ and $Ce_{1-x}Zr_xVO_4$ catalysts during the whole temperature window. Among them, the $CeVO_4$ showed the lowest N_2 selectivity which started to decrease at about 300 °C, and down to 74.6% at 400 °C. The selectivity of the $Ce_{1-x}Zr_xVO_4$ catalysts was kept close to 100% during the whole temperature range, indicating that the doping of Zr could significantly improve the selectivity, even with very small amount of Zr.

The NH_3 oxidation over different $Ce_{1-x}Zr_xVO_4$ catalysts was shown in Fig. S1a. It was found out that the oxidation of NH_3 became obvious at higher temperature. With the amount of Zr increasing, the light-off temperature of NH_3 oxidation decreased, namely 375, 350, 325 to 275 °C for $Ce_{0.20}Zr_{0.80}VO_4$, $Ce_{0.30}Zr_{0.70}VO_4$, $Ce_{0.50}Zr_{0.50}VO_4$, $Ce_{0.20}Zr_{0.80}VO_4$, respectively. Interestingly, those temperatures were coincident with the highest temperatures of the working temperature window in Fig. 1a, implying that the unwanted oxidation of NH_3 caused the decline of catalytic activity at high temperature when the doping amount of Zr was too high [27]. The experiment of oxidation of NO to NO_2 has been performed (Fig. S1b). The oxidation of NO was very low for $CeVO_4$, while the oxidation of NO to NO_2 increased with the Zr addition. Among all the samples, $Ce_{0.85}Zr_{0.15}VO_4$ exhibited the highest NO oxidation for 40% at 300 °C, suggesting that the high conversion of NO to NO_2, namely "fast SCR", were beneficial to the NH_3-SCR reaction.

Since the $Ce_{0.85}Zr_{0.15}VO_4$ catalyst exhibited excellent NO_x conversion and N_2 selectivity, it was chosen to systematically study the NH_3-SCR performance. We firstly studied the NO conversion under different GHSVs which is very crucial for the practical application (Fig. 2). It was found that the $Ce_{0.85}Zr_{0.15}VO_4$ catalyst showed over 80% NO conversion in a wide temperature range from 175 °C to 350 °C under a GHSV of 100,000 h^{-1}. Noticeably, the temperature window (180–350 °C) was still kept when the GHSV increased to as high as 200,000 and 400,000 h^{-1}. The results indicate that the $Ce_{0.85}Zr_{0.15}VO_4$ catalyst exhibit an excellent performance under very high GHSV and is a promising catalyst for practical use.

The stability of $Ce_{0.85}Zr_{0.15}VO_4$ catalyst was also tested both at 110 and 190 °C using the same feed gases in the activity measurements. The $Ce_{0.85}Zr_{0.15}VO_4$ catalyst was found quite stable. The NO conversion only decreased 2% during the 30 h of SCR reaction as shown in Fig. 3a. The TEM and XRD results (Fig. S2) further proved

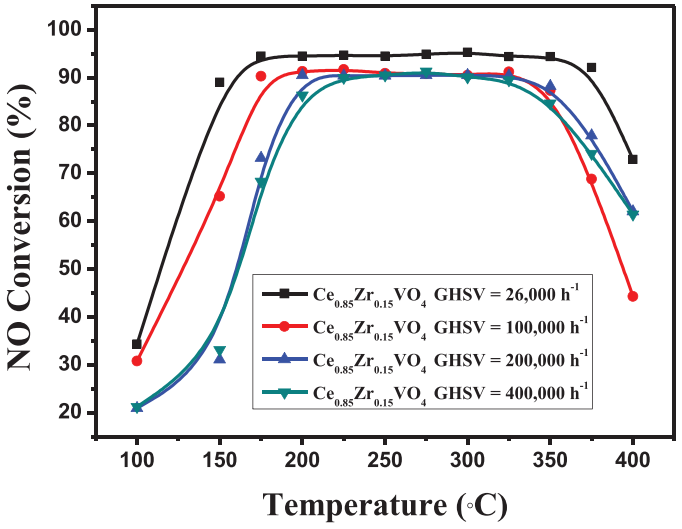

Fig. 2. NH_3-SCR activity of $Ce_{0.85}Zr_{0.15}VO_4$ catalyst under different GHSV (26,000, 100,000, 200,000 and 400,000 h^{-1}). Reaction conditions: [NO] = [NH_3] = 500 ppm, [O_2] = 5%, and N_2 balance.

that the nanorod morphology of the $Ce_{0.85}Zr_{0.15}VO_4$ catalyst is still maintained and the structure of the catalyst is retained as $CeVO_4$ as well after the stability test.

Since a certain amount of H_2O and SO_2 usually exist in the exhaust and also have a strong effect on the performance of the catalysts. The SO_2/H_2O durability was further investigated. Fig. 3b shows the NO conversion tested as a function of time in the presence of 8 vol% H_2O at 190 °C for the $Ce_{0.85}Zr_{0.15}VO_4$ catalyst. Obviously, the performance of $Ce_{0.85}Zr_{0.15}VO_4$ catalyst was not affected by the introduction of H_2O. The introduction of 200 ppm SO_2 into the reaction atmosphere resulted in a decrease of NO conversion from 94.5% to 62.8% as shown in Fig. 3c. However, the NO conversion could be recovered to 87.4% after removing the supply of SO_2. Similarly, the SO_2/H_2O durability test results in Fig. 3d shows that the NO conversion of $Ce_{0.85}Zr_{0.15}VO_4$ catalyst had a decrease from 95.3% to 57.9%, but the NO conversion was recovered to 76.9% after cutting off the supply of H_2O and SO_2. According to the previous studies, the activity decline might be caused by the generation of ammonium sulfate species and blocking the active sites of the catalysts surface [28,29]. Therefore, the $Ce_{0.85}Zr_{0.15}VO_4$ catalyst is highly resistant and reversible to both H_2O and SO_2.

Above results have demonstrated that the Zr doped $CeVO_4$ catalyst exhibited excellent NH_3-SCR activity, N_2 selectivity, stability and SO_2/H_2O durability in a wide temperature range. Very importantly, the above performance was achieved at a wide range

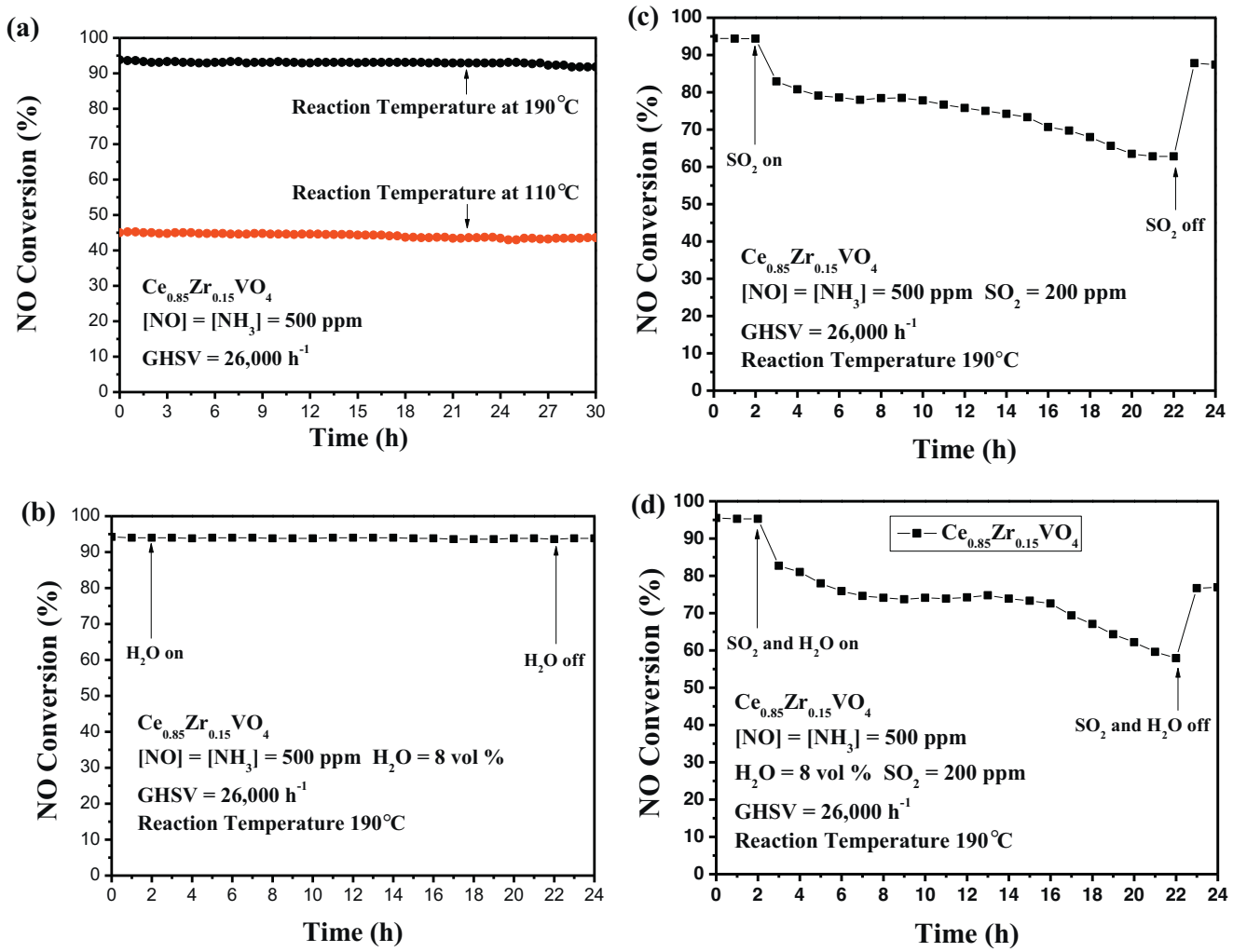

Fig. 3. (a) Stability test at 110 and 190 °C for 30 h (b) H_2O durability test (c) SO_2 durability test and (d) H_2O/SO_2 durability test of the $Ce_{0.85}Zr_{0.15}VO_4$ catalysts at 190 °C for 24 h.

Table 1
The corresponding content and the molar ratios of Ce and Zr over the $CeVO_4$ and $Ce_{1-x}Zr_xVO_4$ (x = 0, 0.10, 0.20, 0.15, 0.50) catalysts.

Samples	Ce (wt%)	Zr (wt%)	V (wt%)	Ce (mmol)	Zr (mmol)	V (mmol)	Ce:Zr
$CeVO_4$	54.41	–	19.65	3.89	–	3.85	–
$Ce_{0.90}Zr_{0.10}VO_4$	50.48	3.46	19.41	3.60	0.38	3.81	9.4:1
$Ce_{0.85}Zr_{0.15}VO_4$	49.87	3.82	18.84	3.56	0.42	3.69	8.4:1
$Ce_{0.80}Zr_{0.20}VO_4$	42.20	2.98	18.68	3.00	0.32	3.66	9.3:1
$Ce_{0.50}Zr_{0.50}VO_4$	29.98	16.05	18.84	2.14	1.70	3.69	1.2:1

of Zr doping amount and could be maintained under very high GHSV, implying that the developed low temperature SCR catalyst is promising for practical use.

3.2. (HR)TEM and SAED analysis

The morphology of the $Ce_{1-x}Zr_xVO_4$ catalysts was investigated by TEM as shown in Fig. 4a–i. The $CeVO_4$ was found in the form of nanorods with lengths between 70 and 250 nm. When the Zr content increased from 0 to 0.30, the morphology of the $Ce_{1-x}Zr_xVO_4$ catalysts maintained as nanorods. The length of $Ce_{1-x}Zr_xVO_4$ nanorods were between 35 and 250 nm. However, the $Ce_{1-x}Zr_xVO_4$ catalysts changed to nanoparticles when further increasing the Zr content.

The formation of $CeVO_4$ nanorods have been well studied somewhere [26]. The $CeVO_4$ nanorods have a tetraganol structure with a preferred growth direction of (0 0 1). This result was also confirmed in this work by the following HRTEM results and SEAD patterns.

Fig. 5 shows the HRTEM images of $CeVO_4$, $Ce_{0.90}Zr_{0.10}VO_4$, $Ce_{0.80}Zr_{0.20}VO_4$ and $Ce_{0.50}Zr_{0.50}VO_4$ catalysts, respectively. Fig. 5a and the insets showed that the $CeVO_4$ nanorods were single crystalline. The clear lattice fringes in the HRTEM images were taken parallel and perpendicular to the c axis. The lattice fringes of (0.49 nm) (0.37 nm) were indexed to (1 0 1) and (2 0 0) crystalline planes, respectively. The SAED diffraction patterns also showed lattice spacing of 0.49 nm and 0.37 nm that can be indexed to the (1 0 1) and (2 0 0) crystalline planes, respectively [26]. Above results demonstrated that the $CeVO_4$ nanorods had a preferred growth direction of (0 0 1) as indicated by the arrow in Fig. 5a. $Ce_{0.90}Zr_{0.10}VO_4$ had a similar growth direction as indicated in Fig. 5b. For both $Ce_{0.80}Zr_{0.20}VO_4$ and $Ce_{0.50}Zr_{0.50}VO_4$ catalysts, nanoparticles were obviously observed according to Fig. 4e and 4 g. The HRTEM images showed that the nanoparticles were also single crystalline. However, they have more growth directions as shown in Fig. 5c and d. Especially, the lattice fringes (0.316 nm) belonging to the typical crystalline planes (−1 0 1) of ZrO_2 were observed, indicating that ZrO_2 were formed when the Zr content increased to 0.5. The following XRD results didn't show the typical diffraction peaks belonging to ZrO_2 over the $Ce_{0.50}Zr_{0.50}VO_4$ catalyst, which was due to the limited amount of ZrO_2.

3.3. XRD and ICP analysis

The crystal structure of $CeVO_4$ and $Ce_{1-x}Zr_xVO_4$ catalysts was further studied by the XRD test (Fig. 6). For the $CeVO_4$ sample, all typical peaks belonging to $CeVO_4$ (JCPDS Card NO.12-0757) were detected. The $Ce_{1-x}Zr_xVO_4$ catalysts (x = 0.05, 0.10, 0.15, 0.20, 0.30, 0.50, 0.70, 0.80) also exhibited the diffraction peaks belonging to $CeVO_4$. No diffraction peaks belonging to other phase were observed. However, the amplified diffraction peak belonging to (2 0 0) indicated that the position slightly shifted to lower degree when the amount of doped Zr increased from 0.05 to 0.50, indicating that Zr had the possibility to dope into the crystalline structure of $CeVO_4$. It is well known that the ion radius of Zr^{4+}, Ce^{3+} and Ce^{4+} were 0.084, 0.114 and 0.097 nm, respectively. One possible was that the doping of Zr induced the transfer of Ce^{4+} to Ce^{3+} in the unit cell. The increase of Ce^{3+} amount was further proved by the XPS results. The crystallographic refinement parameters of $Ce_{1-x}Zr_xVO_4$ were given in Table S1. All the single phase $Ce_{1-x}Zr_xVO_4$ ($0 < x < 0.50$) exhibited a tetragonal structure and the space group of these samples was I41/amd (1 4 1). The unit cell volume increased with the amount of Zr increasing. And both a and c were gradually increasing within the limit of solid solution. This was probably due to the doping of Zr in the crystalline structure. ZrO_2 were observed when the Zr content increased to 0.7 and higher, indicating that the solid solution was hard to form under this condition.

The ICP analysis was conducted to determine the elemental components of the samples. The actual compositions and the molar ratio of Ce and Zr of the investigated materials are summarized in Table 1. It can be seen that the Ce/Zr ratios of $Ce_{0.90}Zr_{0.10}VO_4$, $Ce_{0.85}Zr_{0.15}VO_4$ and $Ce_{0.50}Zr_{0.50}VO_4$ were 9.4:1, 8.4:1, 1.2:1, respectively, close to that of the reactants. The only exception was $Ce_{0.80}Zr_{0.20}VO_4$. Here, the Ce/Zr molar ratio of about 9.3:1 was much higher than the designed number 4:1, which was probably due to part of the Zr were failed to dope into the crystalline structure of $CeVO_4$.

3.4. Visible Raman spectroscopy

The structural information of $Ce_{1-x}Zr_xVO_4$ catalysts were further studied by vis-Raman spectroscopy (Fig. 7). The typical bands for $CeVO_4$ were located at 260, 369, 460, 768 and 836 cm^{-1}. The Raman band at 836 cm^{-1} was assigned to A_{1g} vanadate symmetric stretching (ν_1), at 768 cm^{-1} to the B_{2g} antisymmetric stretching of vanadates (ν_3), at 460 and 369 cm^{-1} to B_{2g} and B_{1g} deformations (ν_4 and ν_3, respectively) [30,31]. The $Ce_{1-x}Zr_xVO_4$ (x = 0.05–0.5) catalysts displayed the similar Raman bands of $CeVO_4$, indicating that the crystalline structure of $Ce_{1-x}Zr_xVO_4$ (x = 0.05–0.5) were kept the same with $CeVO_4$. However, the Raman band at 836 cm^{-1} obviously shifted to higher wavenumbers, which was probably due to the doping of Zr into crystalline structure.

Interestingly, two new bands at 925 and 984 cm^{-1} were observed over $Ce_{0.30}Zr_{0.70}VO_4$ and $Ce_{0.20}Zr_{0.80}VO_4$, respectively. The band at 915–950 cm^{-1} was assigned to the polymerized V—O—V stretching mode. The band at ~990 cm^{-1} was corresponding to the terminal of V=O groups of bulk V_2O_5. These results indicated that vanadium species were agglomerated to form V_2O_5 on the surface of the $Ce_{0.30}Zr_{0.70}VO_4$ and $Ce_{0.20}Zr_{0.80}VO_4$ catalysts [32–34]. However, the V_2O_5 was not detected by XRD probably due to the V_2O_5 were amorphous or highly dispersed over the nanoparticles. Besides, according to the XRD results, ZrO_2 were formed when the Zr content increased to 0.7 and higher. The typical bands of ZrO_2 located at 465 and 622 cm^{-1} were not obvious. The different results from XRD and vis-Raman spectroscopy could be explained as follows. Since the $Ce_{1-x}Zr_xVO_4$ catalysts have strong absorption in the visible region, the vis-Raman spectroscopy might be more surface-sensitive compared with XRD. Therefore, the surface species V_2O_5 were not detected by XRD but observed by vis-Raman spectroscopy. On the contrary, the bulk ZrO_2 was easily detected by XRD while difficultly observed by vis-Raman spectroscopy.

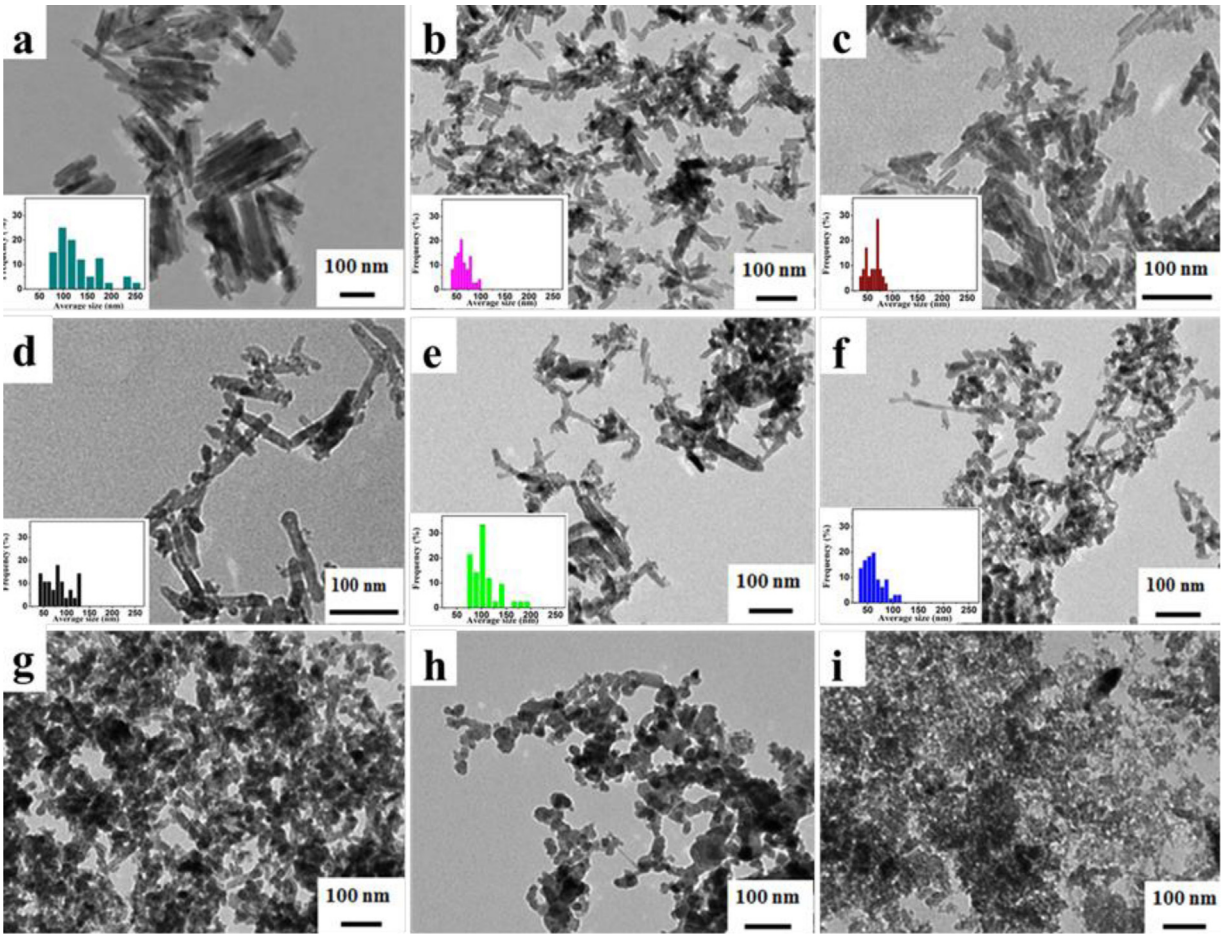

Fig. 4. TEM images and particle size distribution of the (a) $CeVO_4$ (b) $Ce_{0.95}Zr_{0.05}VO_4$ (c) $Ce_{0.90}Zr_{0.10}VO_4$ (d) $Ce_{0.85}Zr_{0.15}VO_4$ (e) $Ce_{0.80}Zr_{0.20}VO_4$ (f) $Ce_{0.70}Zr_{0.30}VO_4$ (g) $Ce_{0.50}Zr_{0.50}VO_4$ (h) $Ce_{0.30}Zr_{0.70}VO_4$ (i) $Ce_{0.20}Zr_{0.80}VO_4$ catalysts.

Table 2
Textural parameters of the $CeVO_4$ and $Ce_{1-x}Zr_xVO_4$ catalysts and corresponding reference samples obtained from N_2 sorption results.

Samples	S_{BET}[a] ($m^2\,g^{-1}$)	V_{BJH}[b] ($cm^3\,g^{-1}$)	D_{BJH}[c] (nm)
$CeVO_4$	32	0.20	3.02
$Ce_{0.95}Zr_{0.05}VO_4$	54	0.25	3.50
$Ce_{0.90}Zr_{0.10}VO_4$	92	0.46	3.48
$Ce_{0.85}Zr_{0.15}VO_4$	96	0.59	3.00
$Ce_{0.80}Zr_{0.20}VO_4$	93	0.67	3.06
$Ce_{0.70}Zr_{0.30}VO_4$	117	0.50	3.05
$Ce_{0.50}Zr_{0.50}VO_4$	113	0.42	2.46
$Ce_{0.30}Zr_{0.70}VO_4$	32	0.33	3.08
$Ce_{0.20}Zr_{0.80}VO_4$	28	0.16	3.06

[a] BET surface area.
[b] BJH desorption pore volume.
[c] Average pore diameter.

3.5. N_2 sorption analysis

Table 2 shows the textural parameters of $CeVO_4$ and $Ce_{1-x}Zr_xVO_4$ catalysts. The BET surface area of the $CeVO_4$ was about 32 $m^2\,g^{-1}$. The surface area rapidly increased to about 92 $m^2\,g^{-1}$ with the doping of Zr content to 0.10. The BET surface area of the $Ce_{1-x}Zr_xVO_4$ catalysts showed an increase firstly and then decrease. The $Ce_{0.70}Zr_{0.30}VO_4$ catalyst had the largest surface area of about 117 $m^2\,g^{-1}$. When the Zr content further increased to higher than 0.3, the BET surface area rapidly decreased. The surface area increased firstly and then decreased, making it easy to combine this trend to the catalytic performance in Fig. 1a. However, the catalytic performance was not governed by the surface area when we carefully analyzed the results. On one hand, $CeVO_4$ and $Ce_{0.30}Zr_{0.70}VO_4$ have similar surface area, but the NO conversion of $Ce_{0.30}Zr_{0.70}VO_4$ is much better than that of $CeVO_4$. Similarly, $Ce_{1-x}Zr_xVO_4$ ($x = 0.1, 0.15, 0.2$) has lower surface area than $Ce_{1-x}Zr_xVO_4$ ($x = 0.3, 0.5$), but $Ce_{1-x}Zr_xVO_4$ ($x = 0.1, 0.15, 0.2$) has better SCR performance than $Ce_{1-x}Zr_xVO_4$ ($x = 0.3, 0.5$). On the other hand, the surface area of $Ce_{0.85}Zr_{0.15}VO_4$ is about three times higher than that of $CeVO_4$. However, the SCR performance of $Ce_{0.85}Zr_{0.15}VO_4$ is still much better than that of $CeVO_4$ when the amount of $Ce_{0.85}Zr_{0.15}VO_4$ decreases to about one fourth during the SCR reactions (GHSV of 100,000–400,000 h^{-1}). The above results suggest that the SCR performance of $CeVO_4$ and $Ce_{1-x}Zr_xVO_4$ catalysts is not governed by the textural parameters but some other factors.

3.6. H_2-TPR analysis

It is well known that the redox property of catalysts is significant in the catalytic cycle of NH_3-SCR reactions. Fig. 8 shows the H_2-TPR results of the $CeVO_4$ and $Ce_{1-x}Zr_xVO_4$ catalysts. Two obvious peaks were observed in the whole reduction process. The first weaker peak below 600 °C can be attributed to reduction of complicated species like Ce^{4+}, Zr^{4+} or surface V^{5+} [8,35–38]. The second peak above 600 °C belonged to the reduction of bulk vanadium species [36,39].

The first reduction peak of the $CeVO_4$ catalyst was very weak and its position at 588 °C was much higher than those of the other

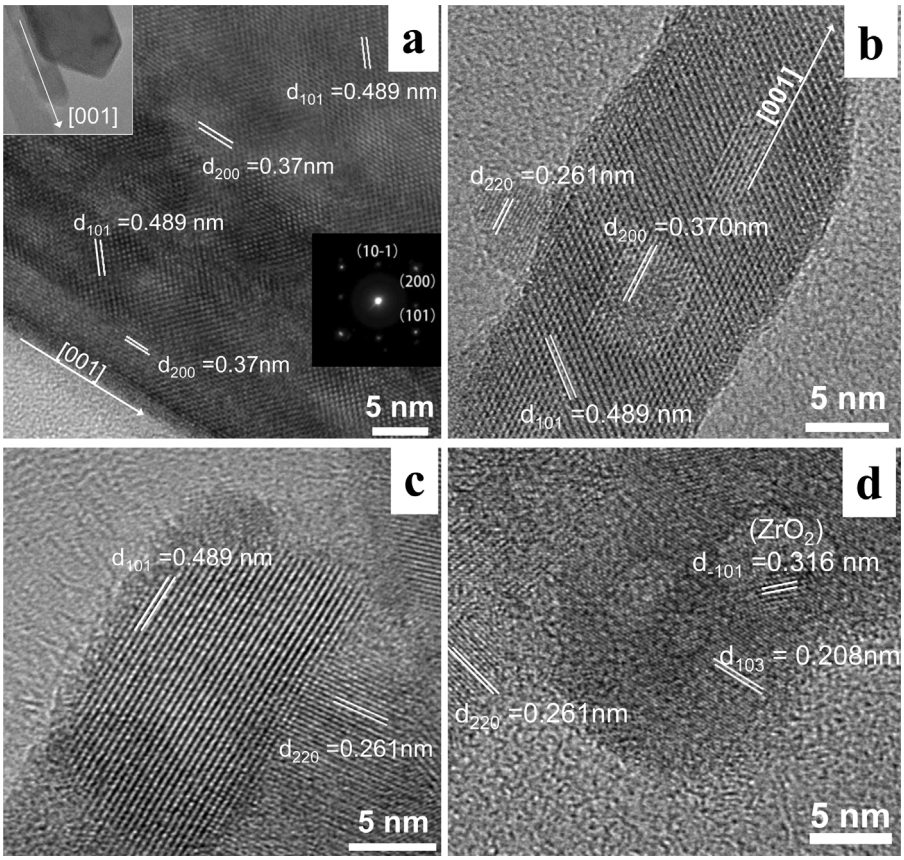

Fig. 5. HRTEM images of the (a) $CeVO_4$, (b) $Ce_{0.90}Zr_{0.10}VO_4$, (c) $Ce_{0.80}Zr_{0.20}VO_4$ and (d) $Ce_{0.50}Zr_{0.50}VO_4$ catalysts. The insets in (a) are the HRTEM image and SAED patterns, respectively.

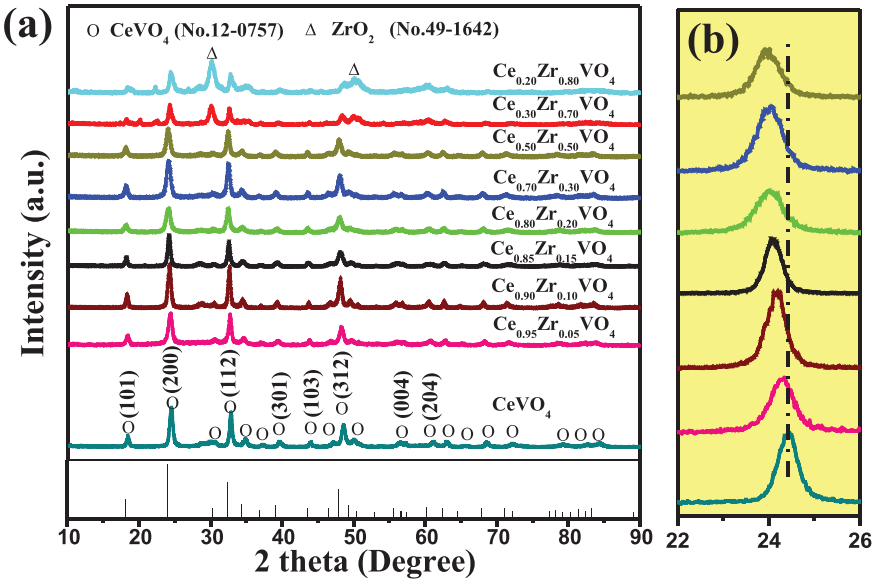

Fig. 6. (a) XRD patterns of the $CeVO_4$ and $Ce_{1-x}Zr_xVO_4$ catalysts. (b) The enlarged part of (a) from 22 to 26°.

$Ce_{1-x}Zr_xVO_4$ catalysts, indicating that the amount of surface vanadium species was very small and hard to be reduced over $CeVO_4$. The positions of the $Ce_{1-x}Zr_xVO_4$ (x = 0.05, 0.10, 0.15, 0.20, 0.30 and 0.50) catalysts moved to lower temperature first and then to higher temperature with the Zr addition. However, all the positions were far lower than 588 °C, implying that the $Ce_{1-x}Zr_xVO_4$ catalysts have better redox properties than $CeVO_4$, and was beneficial to the catalytic cycle of NH_3-SCR reactions. For example, $Ce_{0.85}Zr_{0.15}VO_4$ showed the lowest reduction temperature of 491 °C and exhibited a superior NH_3-SCR performance. When the amount of Zr increased to higher than 0.5, the second peak obviously moved to lower temperature and integrated into the first reduction position. This change might be caused by the accumulation of vanadium species over the surface of the nanoparticles, as illustrated by the

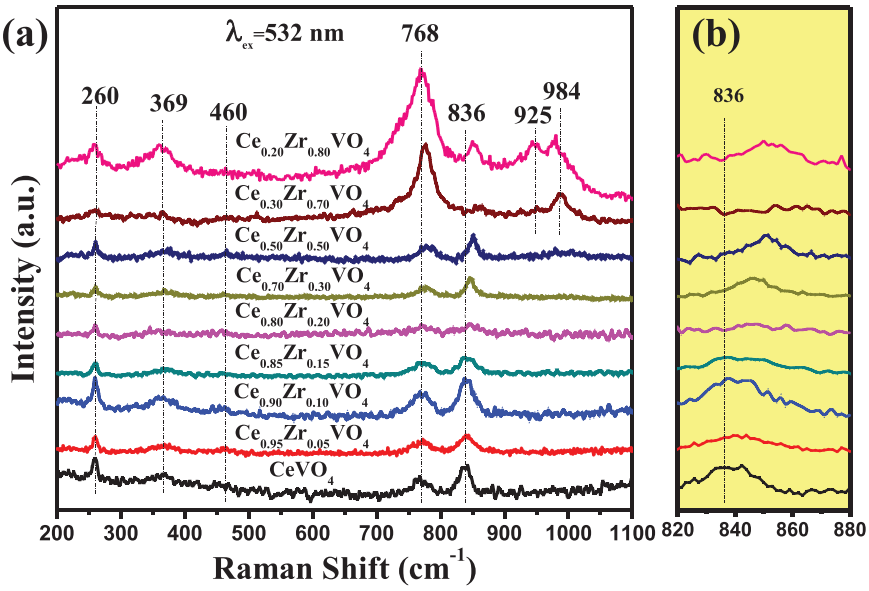

Fig. 7. (a) Visible Raman spectra of the $CeVO_4$ and $Ce_{1-x}Zr_xVO_4$ catalysts. (b) The enlarged part of (a) from 820 to 880 cm^{-1}.

vis-Raman results. The surface vanadium species were prone to be reduced.

It has been widely accepted that the vanadium species are very important to the oxidation of NO during the SCR reactions [40,41]. The evolution of vanadium species over the surface would address the change of NO conversion and the N_2 selectivity. The doping of proper amount of Zr causes the exposure of more vanadium species on the surface, thus promoting the performances during the SCR reactions. However, with the amount of Zr increased to the critical point, the phase separation occurred and overmuch surface vanadium species were exposed, which would cause the unexpected NH_3 unselective oxidation, and thus decrease both the NO conversion and the N_2 selectivity.

3.7. NH_3-TPD analysis

Since the NH_3-TPD is a crucial process in the NH_3-SCR reactions, it was performed to study the adsorption and activation of NH_3 on the active sites of the catalyst surface. Normally, the NH_3 desorption peaks below 240 °C assigned to partially ionic NH_4^+ belonged to weak Brønsted acid sites. The peaks from 250 to 500 °C corresponded to the desorption of NH_4^+ bounded to strong Brønsted acid sites and coordinated NH_3 bounded to Lewis acid sites [42]. Since it is very difficult to identify the strong Brønsted acid sites and Lewis acid sites according to the NH_3-TPD profiles, both the acid sites were then ascribed to strong acid sites.

Fig. 9 shows that all the NH_3-TPD profiles of the $Ce_{1-x}Zr_xVO_4$ catalysts could be divided into three peaks. According to the description above, the peaks between 100 and 240 °C (175 and 228 °C for $CeVO_4$, 176 °C for $Ce_{0.95}Zr_{0.05}VO_4$, 226 °C for $Ce_{0.90}Zr_{0.10}VO_4$, 212 °C for $Ce_{0.85}Zr_{0.15}VO_4$, 190 °C for $Ce_{0.80}Zr_{0.20}VO_4$, 200 °C for $Ce_{0.70}Zr_{0.30}VO_4$, 198 °C for $Ce_{0.50}Zr_{0.50}VO_4$, 195 °C for $Ce_{0.30}Zr_{0.70}VO_4$, 194 °C for $Ce_{0.20}Zr_{0.80}VO_4$) can be ascribed to the desorption of partial ionic NH_4^+ belonged to weak Brønsted acid sites [43–45]. The peaks at 250–500 °C (425 °C for $CeVO_4$, 285 and 428 °C for $Ce_{0.95}Zr_{0.05}VO_4$, 340 and 490 °C for $Ce_{0.90}Zr_{0.10}VO_4$, 328 and 485 °C for $Ce_{0.85}Zr_{0.15}VO_4$, 275 and 445 °C for $Ce_{0.80}Zr_{0.20}VO_4$, 308 and 460 °C for $Ce_{0.70}Zr_{0.30}VO_4$, 272 and 350 °C for $Ce_{0.50}Zr_{0.50}VO_4$, 295 and 420 °C for $Ce_{0.30}Zr_{0.70}VO_4$, 260 and 410 °C for $Ce_{0.20}Zr_{0.80}VO_4$) correspond to the desorption of NH_4^+ bounded to strong Brønsted acid sites and coordinated NH_3 bounded to Lewis acid sites [42,46,47].

The areas of NH_3 desorption bands ascribed to the strong acid sites, weak acid sites and the total acid sites were normalized to that of $CeVO_4$ and were summarized in Fig. S3a. It is obvious that the amounts of the weak acid sites, strong acid sites and the total acid sites increased firstly and decreased thereafter. The total amount of acid sites over $Ce_{1-x}Zr_xVO_4$ (x = 0.10, 0.15, 0.20 and 0.30) increased about 9 times compared with that over $CeVO_4$. To exclude the influences of surface area, the above results also normalized to the surface area as shown in Fig. S3b. Interestingly, the evolution of acid sites still had the similar trend compared with the NO conversion in Fig. 1a, implying that the increase of acid amount is a crucial factor that affects the SCR performance. According to the literatures, the introduction of Zr could significantly enhance the acid sites which were beneficial to the SCR reactions [48–50]. Therefore, the increase of surface acid sites might be one of the major reasons that promoted the SCR performances by the doping of Zr species.

3.8. NO_x-TPD analysis

The NO_x-TPD results are shown in Fig. 10. According to the literature, the peaks below 200 °C can be ascribed to the desorption of physisorbed NO_x and monodentate nitrate species, and the peaks above 200 °C were due to the decomposition of bridging nitrate species and bidentate nitrate species [51,52].

Accordingly, the peaks below 200 °C (97 and 170 °C for $CeVO_4$, 98 and 150 °C for $Ce_{0.95}Zr_{0.05}VO_4$, 105 and 162 °C for $Ce_{0.90}Zr_{0.10}VO_4$, 102 and 160 °C for $Ce_{0.85}Zr_{0.15}VO_4$ and for $Ce_{0.80}Zr_{0.20}VO_4$, 103 and 165 °C for $Ce_{0.70}Zr_{0.30}VO_4$ and $Ce_{0.50}Zr_{0.50}VO_4$, 100 and 165 °C for $Ce_{0.30}Zr_{0.70}VO_4$, 90 and 150 °C for $Ce_{0.20}Zr_{0.80}VO_4$) can be ascribed to the desorption of physisorbed NO_x and monodentate nitrate species [53]. The peaks above 200 °C (320 °C for $CeVO_4$, 236 and 395 °C for $Ce_{0.95}Zr_{0.05}VO_4$, 255 and 370 °C for $Ce_{0.90}Zr_{0.10}VO_4$, 255 and 375 °C for $Ce_{0.85}Zr_{0.15}VO_4$, 242 and 350 °C for $Ce_{0.80}Zr_{0.20}VO_4$, 256 and 360 °C for $Ce_{0.70}Zr_{0.30}VO_4$, 278 °C for $Ce_{0.50}Zr_{0.50}VO_4$, 255 and 342 °C for $Ce_{0.30}Zr_{0.70}VO_4$, 238 and 360 °C for $Ce_{0.20}Zr_{0.80}VO_4$) belong to the decomposition of bridging nitrate species and bidentate nitrate species.

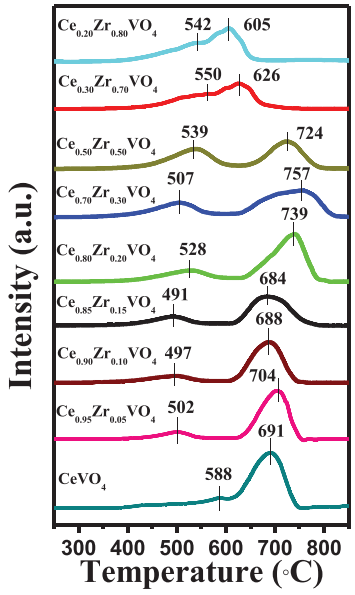

Fig. 8. H_2-TPR profiles of the $CeVO_4$ and $Ce_{1-x}Zr_xVO_4$ catalysts.

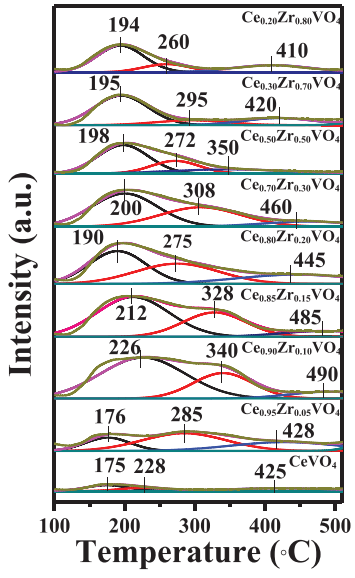

Fig. 9. NH_3-TPD profiles of the $CeVO_4$ and $Ce_{1-x}Zr_xVO_4$ catalysts.

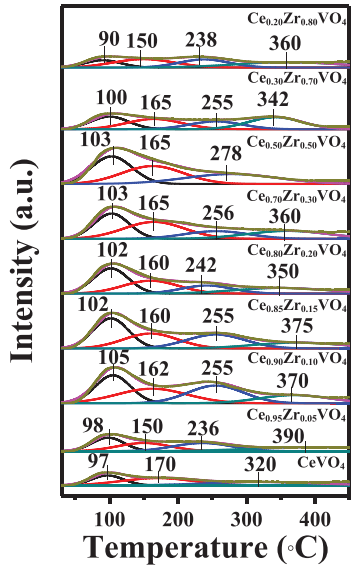

Fig. 10. NO_x-TPD profiles of the $CeVO_4$ and $Ce_{1-x}Zr_xVO_4$ catalysts.

Table 3
The corresponding concentration ratios and binding energies over the $CeVO_4$ and $Ce_{1-x}Zr_xVO_4$ catalysts.

Samples	$O_\alpha/(O_\alpha+O_\beta)$(%)	Ce^{3+}/Ce(%)	V $2p_{3/2}$(eV)	Zr $3d_{5/2}$(eV)
$CeVO_4$	37.59	54.36	516.70	–
$Ce_{0.85}Zr_{0.15}VO_4$	52.14	70.00	516.90	181.90
$Ce_{0.50}Zr_{0.50}VO_4$	48.64	60.57	517.10	181.60
$Ce_{0.20}Zr_{0.80}VO_4$	43.09	64.28	517.30	181.60

The areas of NO_x desorption bands over $Ce_{1-x}Zr_xVO_4$ were normalized to that over $CeVO_4$ as shown in Fig. S4a. The evolution of NO_x desorption amounts for all the nitrate species also showed an increase firstly and a decrease thereafter. However, if they were further normalized to the surface area (Fig. S4b), this trend did not exist anymore. Therefore, the doped Zr do not have obvious influence on the adsorption of NO_x, and the SCR performance over $Ce_{1-x}Zr_xVO_4$ catalysts.

3.9. XPS analysis

The surface compositions and chemical states of the elements were investigated by XPS. The obtained XPS spectra of O 1s, V 2p, Zr 3d and Ce 3d are shown in Fig. 11.

Fig. 11a shows the O 1s bands of different catalysts by curve-fitting procedure. The O 1s XPS spectra were fitted into two peaks. The sub-bands at lower binding energy (529.6–530.1 eV) were assigned to the lattice oxygen O^{2-} (denoted O_β) [54,55], and the sub-bands at higher binding energy (531.4–532.5 eV) were ascribed to the surface absorbed oxygen (denoted O_α) [28,52,56], such as O_2^{2-} (or O^-) attributing to defect oxide or hydroxyl-like groups. The corresponding peak-fitting results of O 1s and the relative concentration ratios of $O_\alpha/(O_\alpha+O_\beta)$ over these catalysts are summarized in Table 3. The $O_\alpha/(O_\alpha+O_\beta)$ ratios of the $CeVO_4$, $Ce_{0.85}Zr_{0.15}VO_4$, $Ce_{0.50}Zr_{0.50}VO_4$ and $Ce_{0.20}Zr_{0.80}VO_4$ were 37.59%, 52.14%, 48.64 and 43.09%, respectively. This result indicated that there were more oxide defects or hydroxyl groups in $Ce_{1-x}Zr_xVO_4$ than that in $CeVO_4$. The surface hydroxyl groups were mainly acidic, supplying more Brønsted acid sites to adsorb NH_3 species and thus promoting the amount of NH_4^+ in the SCR reaction. Thus the addition of Zr could increase the acid sites which were corresponding to the NH_3-TPD results [57]. Besides, the $O_\alpha/(O_\alpha+O_\beta)$ ratio of the $Ce_{0.85}Zr_{0.15}VO_4$ was much higher than that of the other catalysts. The $Ce_{0.85}Zr_{0.15}VO_4$ catalyst also showed better performance in the SCR reaction, suggesting that the present surface oxygen was beneficial to the enhancement of the SCR activity. Since surface oxygen O_α has high mobility than the lattice oxygen O_β, O_α is more active in oxidation of NO to NO_2, therefore facilitates the "fast SCR" reaction as the presence of NO_2 in the gas mixture is beneficial to the SCR reaction on the catalysts [58,59]. Moreover, the $O_\alpha/(O_\alpha+O_\beta)$ ratios increased with the introduction of Zr compared with $CeVO_4$. The possible reason is that the doping of Zr^{4+} results in the generation of low-valence state metal cations, which can create the oxygen vacancy, charge imbalance and unsaturated chemical bond on the surface of these catalysts [48].

The XPS results of V 2p and Zr 3d of the $CeVO_4$, $Ce_{0.85}Zr_{0.15}VO_4$, $Ce_{0.50}Zr_{0.50}VO_4$ and $Ce_{0.20}Zr_{0.80}VO_4$ are shown in Fig. 11b and c. The binding energies of V $2p_{3/2}$ over $CeVO_4$ and $Ce_{1-x}Zr_xVO_4$ catalysts located at around 516.7 eV, indicating that the main oxidation state of vanadium species were V^{5+}. It was also found that the position of V $2p_{3/2}$ was shifted toward higher binding energy with the increase of Zr amount. For the Zr species, the binding energies of Zr $3d_{5/2}$ over $CeVO_4$ and $Ce_{1-x}Zr_xVO_4$ catalysts located at around 181.6 eV, indicating that the main oxidation states of zirconium species were Zr^{3+}. Here, the oxidation state was abnormal which was probably attributed to the unusual coordination envi-

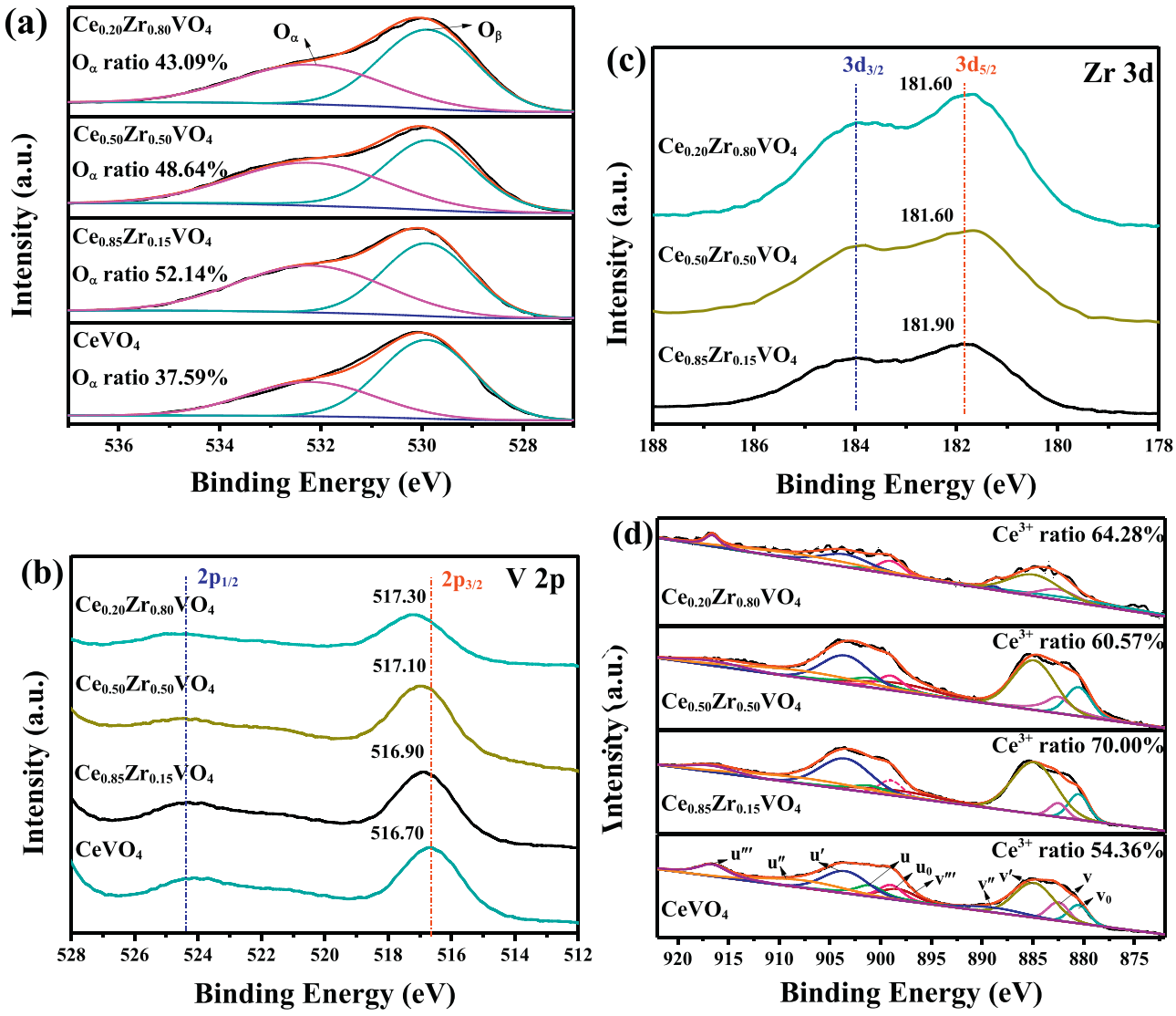

Fig. 11. XPS spectra for (a) O 1s (b) V 2p (c) Zr 3d and (d) Ce 3d of the $CeVO_4$ and $Ce_{1-x}Zr_xVO_4$ catalysts.

ronment of Ce. Since the main state of Ce in $Ce_{1-x}Zr_xVO_4$ is 3+, the Zr designed to replace Ce might also in the main form of 3+. Besides, according to the literature, Zr 3+ also possibly exists in solid solution in some cases [60]. Meanwhile, the peak positions of Zr 3d for $Ce_{0.85}Zr_{0.15}VO_4$, $Ce_{0.50}Zr_{0.50}VO_4$ and $Ce_{0.20}Zr_{0.80}VO_4$ were shifted toward lower binding energies, suggesting that some Zr^{4+} could be reduced to Zr^{3+}. The simultaneous shift of V $2p_{3/2}$ to higher binding energy and Zr $3d_{5/2}$ to lower binding energy was possibly due to the transformation of electrons from V ion to Zr ion. This phenomenon was probably due to the electron interaction between the introduced metal Zr and V ($V^{4+} + Zr^{4+} \leftrightarrow V^{5+} + Zr^{3+}$), similar to other reports [55,60,61].

As shown in Fig. 11d, the curves of Ce 3d spectra were fitted with ten peaks corresponding to five pairs of spin-orbit doublets. The ten peaks were v_o (880.5 eV), v (882.5 eV), v' (884.9 eV), v'' (888.8 eV), v''' (898.3 eV), u_o (899.0 eV), u (901.1 eV), u' (903.5 eV), u'' (907.5 eV) and u''' (916.6 eV) in turn. These series of peaks denoted v and u belonged to the Ce $3d_{5/2}$ and Ce $3d_{3/2}$ spin-orbit components, respectively [62,63]. The peaks labelled by v_o, v', u_o and u' are assigned to the characteristic peaks of Ce^{3+} species, while those denoted by v, v'', v''', u, u'' and u''' are belonged to Ce^{4+} species [64–67]. The relative percentages of the cerium species were semi-quantitatively estimated by the area ratios of Ce^{3+}/Ce shown in Table 3. The 3d XPS spectra reveal the coexistence of Ce^{3+} and Ce^{4+} species. After the introduction of Zr, the concentration of Ce^{3+} was enhanced. The calculated surface Ce^{3+}/Ce ratio was larger on the $Ce_{0.85}Zr_{0.15}VO_4$ (70.00%) than that on the other catalysts. Meanwhile, the Ce^{3+}/Ce ratio in $Ce_{1-x}Zr_xVO_4$ was larger than that in $CeVO_4$. This was probably due to that the doped Zr caused some electronic interaction between Ce and Zr, namely $Ce^{4+} + Zr^{3+} \leftrightarrow Ce^{3+} + Zr^{4+}$.

To sum up, the Zr addition results in dual redox reactions ($V^{4+} + Zr^{4+} \leftrightarrow V^{5+} + Zr^{3+}$ and $Ce^{4+} + Zr^{3+} \leftrightarrow Ce^{3+} + Zr^{4+}$), creating the charge imbalance and oxygen vacancy on the surface, and meanwhile making the vanadium species more active for NO oxidation. The increase of oxygen vacancy and redox property are obviously beneficial to the SCR reactions.

3.10. In-situ *DRIFTS studies*

In-situ DRIFTS were conducted at 150 °C to investigate the influence of Zr addition on NH_3 adsorption and the results are shown in Fig. 12a. The adsorption of NH_3 species over $CeVO_4$ was quite weak which was corresponding to the results of NH_3-TPD. No obvious bands ascribed to adsorbed NH_3 species were detected on $CeVO_4$. The situation was obviously changed with the doping of

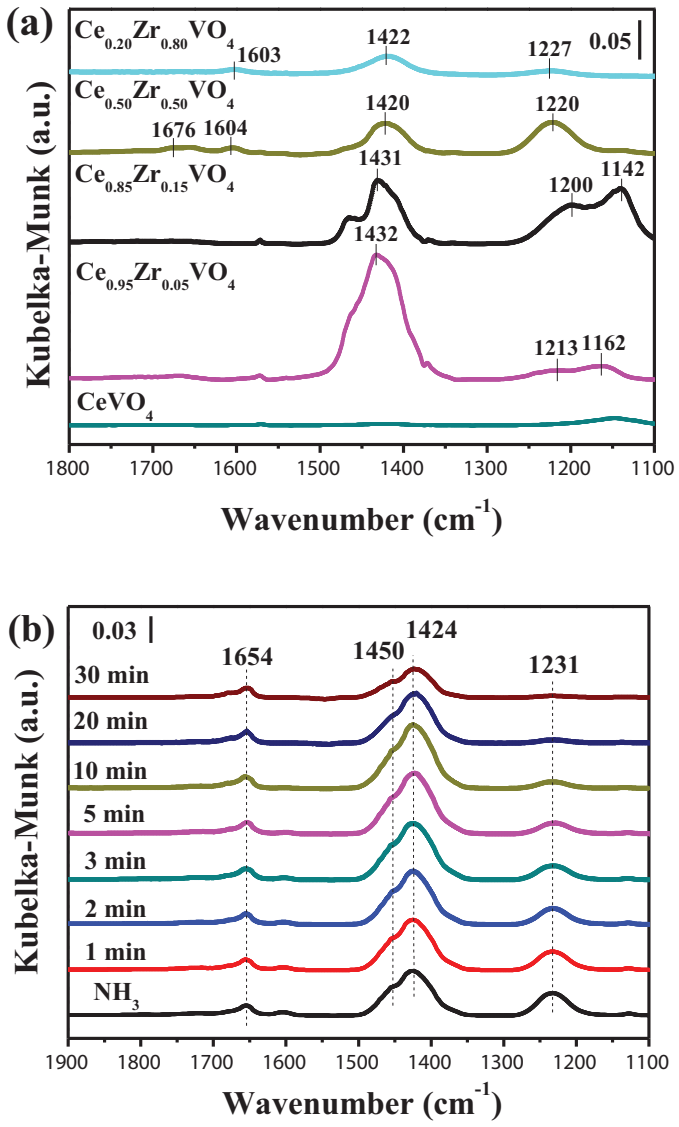

Fig. 12. *In-situ* DRIFTS of (a) NH_3 adsorption at 150 °C on $CeVO_4$, $Ce_{0.95}Zr_{0.05}VO_4$, $Ce_{0.85}Zr_{0.15}VO_4$, $Ce_{0.50}Zr_{0.50}VO_4$ and $Ce_{0.20}Zr_{0.80}VO_5$ and (b) $NO + O_2$ reacted with pre-adsorbed NH_3 species at 150 °C on $Ce_{0.85}Zr_{0.15}VO_4$.

Zr. The bands belonging to chemisorbed species on both Brønsted acid sites and Lewis acid sites were clearly observed, indicating that the doping of Zr obviously increased the amount of acid sites as illustrated by the NH_3-TPD results. The bands at 1420–1450 (1432 for $Ce_{0.95}Zr_{0.05}VO_4$, 1431 for $Ce_{0.85}Zr_{0.15}VO_4$, 1420 for $Ce_{0.50}Zr_{0.50}VO_4$ and 1422 for $Ce_{0.20}Zr_{0.80}VO_4$) cm^{-1} and 1650–1680 (1676 for $Ce_{0.50}Zr_{0.50}VO_4$) cm^{-1} can be ascribed to the asymmetric bending vibration of N—H bond in NH_4^+ chemisorbed on Brønsted acid sites [58,68–72], while the bands at 1140–1180 (1162 for $Ce_{0.95}Zr_{0.05}VO_4$, 1142 for $Ce_{0.85}Zr_{0.15}VO_4$) cm^{-1}, 1195–1232 (1213 for $Ce_{0.95}Zr_{0.05}VO_4$, 1200 for $Ce_{0.85}Zr_{0.15}VO_4$, 1220 for $Ce_{0.50}Zr_{0.50}VO_4$ and 1227 for $Ce_{0.20}Zr_{0.80}VO_4$) cm^{-1} and 1595–1610 (1604 for $Ce_{0.50}Zr_{0.50}VO_4$ and 1603 for $Ce_{0.20}Zr_{0.80}VO_4$) cm^{-1} are attributed to the asymmetric and symmetric bending vibration of N—H bond in NH_3 coordinately belonged to Lewis acid sites [52,69,72–74]. The band intensities of the adsorbed NH_3 species attributed to both Brønsted acid sites and Lewis acid sites increased firstly and then decreased, which was absolutely in accord with the NH_3-TPD results. It is obvious that the intensity of Lewis acid sites showed an increase first and decrease later. The increase was attributed to the increase of Zr amount which was favourable to the formation of Lewis acid sites. The decrease was due to the increase of relative vanadium species on the surface as demonstrated above [7,70].

The *in-situ* DRIFTS of $NO + O_2$ reacted with pre-adsorbed NH_3 species were investigated as a function of time to confirm the reactivity of adsorbed NH_3 species in SCR reaction on $Ce_{0.85}Zr_{0.15}VO_4$ samples (Fig. 12b). After the introduction of $NO + O_2$ at 150 °C, the adsorbed NH_3 species including coordinated NH_3 (1231 cm^{-1} for $Ce_{0.85}Zr_{0.15}VO_4$) and ionic NH_4^+ (1424, 1450 and 1654 cm^{-1} for $Ce_{0.85}Zr_{0.15}VO_4$) all showed a decrease in intensity due to the reaction with NO_x, indicating that both Lewis and Brønsted acid sites on the $Ce_{0.85}Zr_{0.15}VO_4$ catalyst contributed to the NH_3-SCR reaction. The intensity of Lewis acid sites decreased much more rapidly than the Brønsted acid sites, which means that the Lewis acid sites over $Ce_{0.85}Zr_{0.15}VO_4$ are much more active than the Brønsted acid sites. Thus, the presence of Lewis acid sites on the surface would be beneficial to the NH_3-SCR reactions.

Combined with the results in Fig. 9 and Fig. 12, it can be concluded that the doping of Zr significantly increased the amount of acid sites, especially the Lewis acid sites. This was one of the major factors to promote the performance during the SCR reactions.

3.11. Promotional effects of zirconium on $CeVO_4$

Above results have demonstrated that the Zr doped $CeVO_4$ catalyst exhibited excellent NH_3-SCR activity, N_2 selectivity, stability and SO_2/H_2O durability in a wide temperature range. Importantly, the above performance was achieved at a wide range of Zr doping amount and could be maintained under very high GHSV, implying that the developed low temperature SCR catalyst is promising for practical use.

The promotional effects of zirconium on $CeVO_4$ for NH_3-SCR reaction were addressed as follows. It has been proved that the doping of Zr into the $CeVO_4$ nanostructure caused the changes of surface area, morphology, crystalline structure, surface property and etc. The surface area of $CeVO_4$ increased with the doping of proper amount of Zr. The SCR reaction might be benefited from this change. However, the surface area of the $Ce_{1-x}Zr_xVO_4$ catalysts was proved to be not the key factor that promoting the SCR performance. The morphology of the $Ce_{1-x}Zr_xVO_4$ catalysts changed from nanorods to nanoparticles with the increase of Zr amount. It seems that the nanorods dominated catalyst exhibited better activity than the nanoparticles dominated catalyst. To address this problem, we further prepared $Ce_{0.85}Zr_{0.15}VO_4$ nanoparticles which also showed very good performance compared to the $Ce_{0.85}Zr_{0.15}VO_4$ nanorods (Fig. S5). Therefore, the SCR performance was not related to the morphology but the composition of the $Ce_{1-x}Zr_xVO_4$ catalysts which was close related to the surface properties.

The crystalline structure was also influenced by the doping of Zr in $CeVO_4$ nanorods. Both the results of XRD and Raman confirmed that Zr has been successfully doped into $CeVO_4$. The diffraction peak belonging to (2 0 0) slightly shift to lower degree and further leading to the increase of crystal cell parameters and unit cell volume. Similar phenomenon has also been reported by other literatures [36,75]. Small amount of Zr caused the increase of interplanar spacing which was possibly due to that the doped Zr resulted in the transfer of Ce^{4+} to Ce^{3+} in the unit cell which was further proved by XPS results. The new formed solid solution was prone to induce the electron interaction between the introduced metal Zr and V ($V^{4+} + Zr^{4+} \leftrightarrow V^{5+} + Zr^{3+}$), Ce and Zr ($Ce^{4+} + Zr^{3+} \leftrightarrow Ce^{3+} + Zr^{4+}$), creating the charge imbalance and oxygen vacancy on the surface, and meanwhile make the vanadium species more active for NO oxidation. The increase of oxygen vacancy and redox property are obviously beneficial to the SCR reactions. However, the heavy doping of Zr caused the new phases of ZrO_2 and surface V_2O_5 which

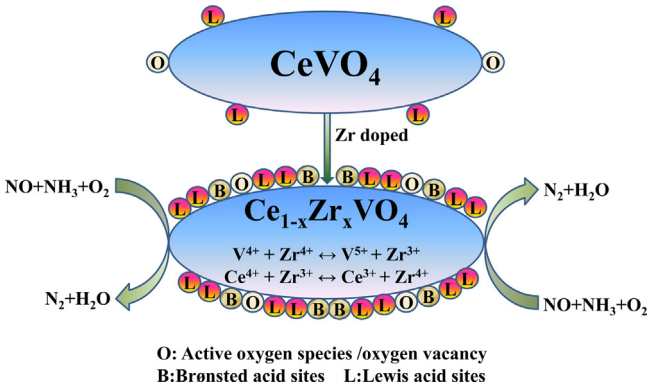

Scheme 1. The relationships of active oxygen species/oxygen vacancy, acid sites and catalytic performance over $Ce_{1-x}Zr_xVO_4$ catalysts.

were harmful to the SCR reactions, especially when their amounts were too high.

As one of the most important surface properties for SCR reaction, the amount of acid sites was critical to the adsorption of NH_3 and the followed SCR reaction cycles. The amount of acid sites for both Brønsted acid sites and Lewis acid sites were found remarkably increased with the doping of Zr [50], which was possibly due to the increase of surface hydroxyl groups and charge imbalance as indicated in the XPS results. However, the formation of excessive vanadium species on the surface causes the increase of Brønsted acid sites. The *in-situ* DRIFTS further indicates that the adsorbed NH_3 species including coordinated NH_3 and ionic NH_4^+ all showed a decrease in intensity due to the reaction with NO_x, which means that both Brønsted acid sites and Lewis acid sites contributed to the NH_3-SCR reactions. But the intensity of Lewis acid sites decreased much more rapidly than the Brønsted acid sites, which means that the Lewis acid sites over $Ce_{0.85}Zr_{0.15}VO_4$ were much more active than the Brønsted acid sites. Besides, the introduction of Zr significantly increased the surface acid sites and the strength of the acids for both Lewis acid and Brønsted acid sites from the results of NH_3-TPD and *in-situ* DRIFTS. It has been demonstrated that both Lewis acid and Brønsted acid were beneficial for the N_2 selectivity at higher temperature [76–78]. Thus, it can be concluded that the doping of Zr significantly increased the amount of acid sites, especially the Lewis acid sites. This was one of the major factors to promote the performance during the SCR reactions, especially the N_2 selectivity.

Based on the results and discussion above, we proposed the promotional effects of zirconium on $CeVO_4$ for NH_3-SCR reaction in Scheme 1. On one hand, the doping of Zr leaded to the enhancement of electron interaction through the redox reactions of $V^{4+} + Zr^{4+} \leftrightarrow V^{5+} + Zr^{3+}$ and $Ce^{4+} + Zr^{3+} \leftrightarrow Ce^{3+} + Zr^{4+}$, thus increasing the active oxygen species/oxygen vacancy. On the other hand, the doping of Zr into $CeVO_4$ also increased both the Brønsted acid sites and Lewis acid sites on the catalysts, which were all beneficial to the NH_3-SCR reactions.

4. Conclusions

In summary, various amounts of Zr were successfully introduced to modify $CeVO_4$ to form the $Ce_{1-x}Zr_xVO_4$ ($x = 0.05$, 0.10, 0.15, 0.20, 0.30, 0.50, 0.70, 0.80) solid solution as low-temperature catalysts for the SCR of NO with NH_3. The $Ce_{1-x}Zr_xVO_4$ exhibited excellent performance at a wide range of Zr doping amount ($x = 0.10$, 0.15, 0.20, 0.30) The temperature window with the NO conversion above 80% ranged from 150 °C to 375 °C and the N_2 selectivity was close to 100% in the whole temperature range. The representative $Ce_{0.85}Zr_{0.15}VO_4$ catalyst also exhibited good H_2O/SO_2 durability and fascinating activity at high gas hourly space velocity (GHSV) of 400,000 h^{-1}. It indicated that the doping of Zr leaded to the enhancement of electron interaction among Ce, Zr and V through the redox reactions of $V^{4+} + Zr^{4+} \leftrightarrow V^{5+} + Zr^{3+}$ and $Ce^{4+} + Zr^{3+} \leftrightarrow Ce^{3+} + Zr^{4+}$, and the redox property and active species were promoted. Besides, the doping of Zr into $CeVO_4$ also increased the BET surface areas and both Brønsted and Lewis acid sites on the catalysts, which were all beneficial to the NH_3-SCR reactions. All the results suggested that the developed $Ce_{1-x}Zr_xVO_4$ catalyst might be a promising catalyst for practical use.

Acknowledgements

This work was financially supported by the National Natural Science Foundation of China (21303099, U1462110), the National Basic Research Program of China (973 Program, 2014CB660803), the Shanghai Municipal Education Commission (14ZZ097, B.3704713001) and the Research Fund for Innovation Program of Shanghai University (K.10040713003).

Appendix A. Supplementary data

Supplementary data associated with this article can be found, in the online version, at http://dx.doi.org/10.1016/j.apcatb.2015.10.052.

References

[1] P.R. Ettireddy, N. Ettireddy, T. Boningari, R. Pardemann, P.G. Smirniotis, J. Catal. 292 (2012) 53–63.
[2] U. Deka, I. Lezcano-Gonzalez, B.M. Weckhuysen, A.M. Beale, ACS Catal. 3 (2013) 413–427.
[3] U. Kamolphop, S.F.R. Taylor, J.P. Breen, R. Burch, J.J. Delgado, S. Chansai, C. Hardacre, S. Hengrasmee, S.L. James, ACS Catal. 1 (2011) 1257–1262.
[4] L. Chen, J. Li, M. Ge, J. Phys. Chem. C 113 (2009) 21177–21184.
[5] L. Zhang, L. Shi, L. Huang, J. Zhang, R. Gao, D. Zhang, ACS Catal. 4 (2014) 1753–1763.
[6] A. Sagar, A. Trovarelli, M. Casanova, K. Schermanz, SAE Int. J. Engines 4 (2011) 1839–1849.
[7] T. Boningari, R. Koirala, P.G. Smirniotis, Appl. Catal. B 127 (2012) 255–264.
[8] T. Boningari, R. Koirala, P.G. Smirniotis, Appl. Catal. B 140 (2013) 289–298.
[9] H.H. Phil, M.P. Reddy, P.A. Kumar, L.K. Ju, J.S. Hyo, Appl. Catal. B 78 (2008) 301–308.
[10] P. Balle, B. Geiger, S. Kureti, Appl. Catal. B 85 (2009) 109–119.
[11] G. Busca, L. Lietti, G. Ramis, F. Berti, Appl. Catal. B 18 (1998) 1–36.
[12] J.P. Dunn, P.R. Koppula, H.G. Stenger, I.E. Wachs, Appl. Catal. B 19 (1998) 103–117.
[13] L. Lietti, I. Nova, G. Ramis, L. Dall'Acqua, G. Busca, E. Giamello, P. Forzatti, F. Bregani, J. Catal. 187 (1999) 419–435.
[14] S. Zhang, Q. Zhong, W. Zhao, Y. Li, Chem. Eng. J. 253 (2014) 207–216.
[15] J. Wang, Z. Yan, L. Liu, Y. Zhang, Z. Zhang, X. Wang, Appl. Surf. Sci. 309 (2014) 1–10.
[16] B. Jiang, B. Deng, Z. Zhang, Z. Wu, X. Tang, S. Yao, H. Lu, J. Phys. Chem. C 118 (2014) 14866–14875.
[17] F. Cao, J. Xiang, S. Su, P. Wang, L. Sun, S. Hu, S. Lei, Chem. Eng. J. 243 (2014) 347–354.
[18] F. Liu, H. He, Z. Lian, W. Shan, L. Xie, K. Asakura, W. Yang, H. Deng, J. Catal. 307 (2013) 340–351.
[19] L. Huang, L. Shi, X. Zhao, J. Xu, H. Li, J. Zhang, D. Zhang, Crystengcomm 16 (2014) 5128.
[20] L. Huang, X. Zhao, L. Zhang, L. Shi, J. Zhang, D. Zhang, Nanoscale 7 (2015) 2743–2749.
[21] M. Casanova, L. Nodari, A. Sagar, K. Schermanz, A. Trovarelli, Appl. Catal. B 176 (2015) 699–708.
[22] A. Marberger, M. Elsener, D. Ferri, A. Sagar, K. Schermanz, O. Kröcher, ACS Catal. 5 (2015) 4180–4188.
[23] G. Wu, J. Li, Z. Fang, L. Lan, R. Wang, M. Gong, Y. Chen, Catal. Commun. 64 (2015) 75–79.
[24] M. Casanova, K. Schermanz, J. Llorca, A. Trovarelli, Catal. Today 184 (2012) 227–236.
[25] M. Casanova, J. Llorca, A. Sagar, K. Schermanz, A. Trovarelli, Catal. Today 241 (2015) 159–168.
[26] J. Liu, L. Wang, X. Sun, X. Zhu, Angew. Chem. Int. Ed. 49 (2010) 3492–3495.
[27] P. Maitarad, J. Han, D. Zhang, L. Shi, S. Namuangruk, T. Rungrotmongkol, J. Phys. Chem. C 118 (2014) 9612–9620.
[28] R. Gao, D. Zhang, X. Liu, L. Shi, P. Maitarad, H. Li, J. Zhang, W. Cao, Catal. Sci. Technol. 3 (2013) 191–199.

[29] W. Xu, H. He, Y. Yu, J. Phys. Chem. C 113 (2009) 4426–4432.
[30] F. Luo, C. Jia, R. Liu, L. Sun, C. Yan, Mater. Res. Bull. 48 (2013) 1122–1127.
[31] M.V. Martínez-Huerta, J.M. Coronado, M. Fernández-García, A. Iglesias-Juez, G. Deo, J.L.G. Fierro, M.A. Bañares, J. Catal. 225 (2004) 240–248.
[32] S. Besselmann, E. Loffler, M. Muhler, J. Mol. Catal. A-Chem. 162 (2000) 401–411.
[33] X. Gao, J.M. Jehng, I.E. Wachs, J. Catal. 209 (2002) 43–50.
[34] I. Giakoumelou, C. Fountzoula, C. Kordulis, S. Boghosian, J. Catal. 239 (2006) 1–12.
[35] X. Gu, J. Ge, H. Zhang, A. Auroux, J. Shen, Thermochim. Acta 451 (2006) 84–93.
[36] M.B. Bellakki, T. Baidya, C. Shivakumara, N.Y. Vasanthacharya, M.S. Hegde, G. Madras, Appl. Catal. B 84 (2008) 474–481.
[37] B. Shen, H. Ma, C. He, X. Zhang, Fuel Process. Technol. 119 (2014) 121–129.
[38] Y. Peng, J. Li, X. Huang, X. Li, W. Su, X. Sun, D. Wang, J. Hao, Environ. Sci. Technol. 48 (2014) 4515–4520.
[39] Y. Shen, Y. Huang, S. Zheng, X. Guo, Z. Chen, L. Peng, W. Ding, Inorg. Chem. 50 (2011) 6189–6194.
[40] J.A. Martín, M. Yates, P. Ávila, S. Suárez, J. Blanco, Appl. Catal. B 70 (2007) 330–334.
[41] M. Koebel, G. Madia, F. Raimondi, A. Wokaun, J. Catal. 209 (2002) 159–165.
[42] K.J. Lee, P.A. Kumar, M.S. Maqbool, K.N. Rao, K.H. Song, H.P. Ha, Appl. Catal. B 142 (2013) 705–717.
[43] F. Liu, K. Asakura, H. He, Y. Liu, W. Shan, X. Shi, C. Zhang, Catal. Today 164 (2011) 520–527.
[44] R.Q. Long, R.T. Yang, J. Catal. 207 (2002) 158–165.
[45] L.S. Cheng, R.T. Yang, N. Chen, J. Catal. 164 (1996) 70–81.
[46] F. Liu, H. He, J. Phys. Chem. C 114 (2010) 16929–16936.
[47] L. Chmielarz, R. Dziembaj, T. Grzybekb, J. Klinik, T. Łojewski, D. Olszewska, A. Wñegrzyn, Catal. Lett. 70 (2000) 51–56.
[48] B. Shen, Y. Wang, F. Wang, T. Liu, Chem. Eng. J. 236 (2014) 171–180.
[49] C.K. Seo, B. Choi, H. Kim, C.H. Lee, C.B. Lee, Chem. Eng. J. 191 (2012) 331–340.
[50] J. Liu, X. Li, Q. Zhao, D. Zhang, Catal. Sci. Technol. 2 (2012) 1711–1718.
[51] Z. Lian, F. Liu, H. He, X. Shi, J. Mo, Z. Wu, Chem. Eng. J. 250 (2014) 390–398.
[52] F. Liu, H. He, Y. Ding, C. Zhang, Appl. Catal. B 93 (2009) 194–204.
[53] J.S. Cha, J.C. Choi, J.H. Ko, Y.K. Park, S.H. Park, K.E. Jeong, S.S. Kim, J.K. Jeon, Chem. Eng. J. 156 (2010) 321–327.
[54] D. Zhang, L. Zhang, L. Shi, C. Fang, H. Li, R. Gao, L. Huang, J. Zhang, Nanoscale 5 (2013) 1127–1136.
[55] X. Yao, L. Zhang, L. Li, L. Liu, Y. Cao, X. Dong, F. Gao, Y. Deng, C. Tang, Z. Chen, L. Dong, Y. Chen, Appl. Catal. B 150 (2014) 315–329.
[56] C. Fang, D. Zhang, S. Cai, L. Zhang, L. Huang, H. Li, P. Maitarad, L. Shi, R. Gao, J. Zhang, Nanoscale 5 (2013) 9199–9207.
[57] Y. Shu, T. Aikebaier, X. Quan, S. Chen, H. Yu, Appl. Catal. B 150 (2014) 630–635.
[58] W. Shan, F. Liu, H. He, X. Shi, C. Zhang, Catal. Today 184 (2012) 160–165.
[59] W. Shan, F. Liu, H. He, X. Shi, C. Zhang, Appl. Catal. B 115 (2012) 100–106.
[60] S. Luo, F. Wang, Z. Shi, F. Xin, Mater. Res. Innov. 13 (2009) 64–69.
[61] Z. Liu, J. Zhu, J. Li, L. Ma, S.I. Woo, ACS Appl. Mater. Interfaces 6 (2014) 14500–14508.
[62] L. Zhang, D. Zhang, J. Zhang, S. Cai, C. Fang, L. Huang, H. Li, R. Gao, L. Shi, Nanoscale 5 (2013) 9821–9829.
[63] F. Larachi, J. Pierre, A. Adnot, A. Bernis, Appl. Surf. Sci. 195 (2002) 236–250.
[64] N. Perret, X. Wang, J.J. Delgado, G. Blanco, X. Chen, C.M. Olmos, S. Bernal, M.A. Keane, J. Catal. 317 (2014) 114–125.
[65] L.E. Gómez, E.E. Miró, A.V. Boix, Int. J. Hydrogen Energy 38 (2013) 5645–5654.
[66] K.N. Rao, P. Venkataswamy, B.M. Reddy, Ind. Eng. Chem. Res. 50 (2011) 11960–11969.
[67] B. Guan, H. Lin, L. Zhu, Z. Huang, J. Phys. Chem. C 115 (2011) 12850–12863.
[68] Z. Wu, B. Jiang, Y. Liu, H. Wang, R. Jin, Environ. Sci. Technol. 41 (2007) 5812–5817.
[69] L. Chen, J. Li, M. Ge, Environ. Sci. Technol. 44 (2010) 9590–9596.
[70] Y. Peng, C. Wang, J. Li, Appl. Catal. B 144 (2014) 538–546.
[71] J. Zhu, F. Gao, L. Dong, W. Yu, L. Qi, Z. Wang, L. Dong, Y. Chen, Appl. Catal. B 95 (2010) 144–152.
[72] T. Gu, R. Jin, Y. Liu, H. Liu, X. Weng, Z. Wu, Appl. Catal. B 129 (2013) 30–38.
[73] L. Zhang, L. Li, Y. Cao, X. Yao, C. Ge, F. Gao, Y. Deng, C. Tang, L. Dong, Appl. Catal. B 165 (2015) 589–598.
[74] M.A. Larrubia, G. Ramis, G. Busca, Appl. Catal. B 30 (2001) 101–110.
[75] S. Mahapatra, R. Vinu, D. Saha, T.N. Guru Row, G. Madras, Appl. Catal. A 361 (2009) 32–41.
[76] A. Burkardt, W. Weisweiler, J.A.A. van den Tillaart, A. Schäfer-Sindlinger, E.S. Lox, Top. Catal. 16 (2001) 369–375.
[77] Z. Si, D. Weng, X. Wu, J. Li, G. Li, J. Catal. 271 (2010) 43–51.
[78] Q. Zhang, Z. Song, P. Ning, X. Liu, H. Li, J. Gu, Catal. Commun. 59 (2015) 170–174.